



HAL
open science

A split Hopkinson pressure bar device to carry out confined friction tests under high pressures

Bastien Durand, Franck Delvare, Patrice Bailly, Didier Picart

► **To cite this version:**

Bastien Durand, Franck Delvare, Patrice Bailly, Didier Picart. A split Hopkinson pressure bar device to carry out confined friction tests under high pressures. *International Journal of Impact Engineering*, 2016, 88, pp.54 - 60. <10.1016/j.ijimpeng.2015.09.002>. <hal-01564488>

HAL Id: hal-01564488

<https://hal.science/hal-01564488v1>

Submitted on 19 Jul 2017

HAL is a multi-disciplinary open access archive for the deposit and dissemination of scientific research documents, whether they are published or not. The documents may come from teaching and research institutions in France or abroad, or from public or private research centers.

L'archive ouverte pluridisciplinaire **HAL**, est destinée au dépôt et à la diffusion de documents scientifiques de niveau recherche, publiés ou non, émanant des établissements d'enseignement et de recherche français ou étrangers, des laboratoires publics ou privés.



HAL Authorization

26 interface are deduced from strain measurements on the Hopkinson bars and on the external
27 face of the confinement tube, and from an analytical model.

28

29 **Keywords:** friction parameter, identification, confinement, split Hopkinson pressure bars

30

31 **1 Introduction**

32

33 Numerical simulations are performed to predict the ignition of confined explosives
34 submitted to accidental impacts [1], [2], [3]. Such impacts are characterised by velocities of
35 several tens of meters per second and are usually called “low-velocity impacts”. These
36 simulations are based on:

- 37 - An elasto-plastic model simulating the macroscopic behaviour, whose parameters are
38 identified from triaxial tests.
- 39 - A thermo-chemical model enabling the calculation of the local heat due to the irreversible
40 macroscopic strain and due to chemical reactions.

41 The parameters of the thermo-chemical model are identified from normalised experimental
42 tests supposed to reproduce accidental situations: the drop-weight test [4], the Steven-test [3],
43 [5], [6], the Susan-test [3] and the Taylor test [7] among others. Unfortunately, numerical
44 simulations of these normalised tests show that the ignition time of the explosive strongly
45 depends on the friction coefficient at the interface between the explosive and the contact
46 materials (generally steel). A test enabling the friction coefficient measurement between steel
47 and explosives under the “low-velocity impacts” conditions has therefore to be designed.

48

49 Numerical simulations display that the “low-velocity impacts” lead to contact
50 pressures reaching 100 MPa and sliding velocities reaching 10 m/s at the interfaces. Few

51 tribometers satisfy these requirements: tribometer with explosively-driven friction [8], target-
52 projectile assembly with oblique impact [9], Hopkinson torsion bars [10], dynamometrical
53 ring with parallelepipedic specimen launched by a gas gun or an hydraulic machine [11] and
54 the friction of a pin on a revolving disc [12], [13]. With these classical tribometers, mainly
55 used on metals and ceramics, the friction samples are tested in simple compression and this
56 configuration is unfortunately not adapted to our situation, as explained above.

57

58 For safety reasons, our friction tests are carried out with an inert material mechanically
59 representative of an explosive. This material is named the I1. The I1 Young's modulus is
60 2 GPa, its Poisson's ratio ν is estimated to 0.4 and its density is 1850 kg/m³ [14]. Its inelastic
61 behavior has been studied by carrying out triaxial compression tests [14]. The material flow
62 when its plasticity threshold has been attained (for the sake of simplicity the maximal stresses
63 obtained using triaxial tests are used to define a plasticity threshold). The plasticity flow
64 threshold is defined by a Drucker-Prager criterion [14]:

65

$$66 \quad (1) \quad \sigma_{mis} - \alpha P < C$$

67 where P is the hydrostatic pressure and σ_{mis} the Von Mises equivalent stress.

68

69 Conventionally, the stress in the I1 is positive in compression and negative in traction.
70 A plastic incompressibility and a perfectly plastic behavior (i.e. C constant) are assumed. The
71 parameters have been determined: $C = 25$ MPa and $\alpha = 0.64$ [14].

72

73 According to relation (1), in the case of a simple compression loading, the maximum
74 axial stress is only 31 MPa. The I1 behavior is quasi-brittle, so when this limit stress is
75 reached, it breaks. The desired 100 MPa pressure cannot therefore be reached with classical

76 tribometers because of the I1 fracture. The material has therefore to be confined during our
77 tests for two following reasons:

- 78 - The behavior of the confined material remains elastic even under high stresses.
- 79 - A confinement situation avoids any fracture to occur when the elasticity limit is reached.

80 A cylindrical I1 sample is thus enclosed in a steel tube. This technique is usually employed to
81 perform compression tests with quasi-uniaxial strain states [14], [15]. Our test bench has to be
82 designed to enables friction to occur between the I1 sample and the steel tube. Our
83 experimental configuration is similar to the compaction tests one [16], [17], [18].

84

85 The Hopkinson bar set-up, its potential performances and the friction identification
86 from a test and from an analytical model are described in section 2. Then, the consistency of
87 this identification is verified in section 3 by performing numerical finite element simulations.

88

89 **2 The Hopkinson bar set-up**

90

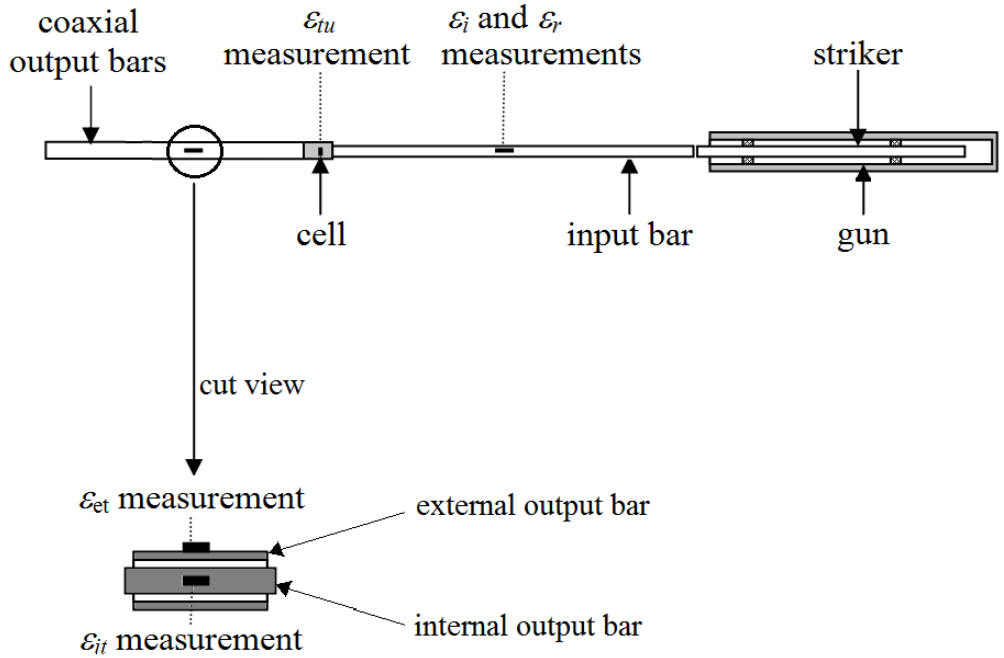
91 **2.1 Design and modeling**

92

93 The Hopkinson bar device used for our friction tests has two coaxial output bars
94 (Figure 1). It consists in an I1 cylindrical sample confined in a steel tube, the sample being
95 inserted between the incident bar (via a plug, see Figure 2) and the internal output bar, and the
96 confinement tube being leant against the external output bar. The high impedance of the
97 external output bar keeps the confinement tube quasi-motionless whereas the impedance of
98 the internal output bar is calculated to reach the desired pressure and the desired velocity at
99 the tube-sample interface. Thus, the steel tube acts both as a confinement, which avoids any

100 fracture in the I1 sample, and as a friction surface. The radial pressure at the confinement
 101 tube – sample interface is generated by the axial compression of the sample.

102



103

104 Figure 1: The Split Hopkinson Pressure Bar device. ϵ_i : incident strain wave, ϵ_r : reflected
 105 strain wave, ϵ_{tu} : strain measured on the confinement tube, ϵ_{et} : external transmitted strain
 106 wave, ϵ_{it} : internal transmitted strain wave.

107

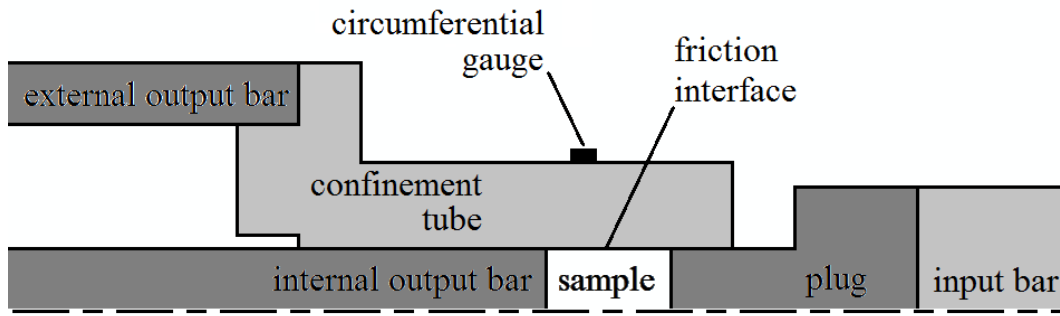
bar	material	Young's modulus	waves celerity	diameters		length
				external	internal	
striker	steel	$E_i = 166 \text{ GPa}$	$C_i = 4555 \text{ m/s}$	$2R_i = 20 \text{ mm}$		1.05 m
input						2.5 m
internal output	aluminum	$E_{io} = 72.8 \text{ GPa}$	$C_{io} = 5092 \text{ m/s}$	$2R_{io} = 10 \text{ mm}$		1.46 m
external output	steel	$E_{eo} = 205 \text{ GPa}$	$C_{eo} = 5162 \text{ m/s}$	$2R_{eoo} = 40 \text{ mm}$	$2R_{ieo} = 30 \text{ mm}$	1.5 m

108 Table 1: Young's moduli, tensile/compressive waves celerities, diameters and lengths of the
109 bars.

110

111 The impact of the striker induces an incident compressive strain wave ε_i in the input
112 bar (Figure 1). Reverberation occurs in the cell (cell details are given on Figure 2), which
113 leads to a reflected strain wave ε_r in the input bar, to a transmitted compressive strain wave ε_{it}
114 in the internal output bar and to a transmitted compressive strain wave ε_{et} in the external
115 output bar. ε_i and ε_r are both measured by a longitudinal strain gauge glued on the input bar,
116 at 1.22 m from the plug interface, where the two waves are separated in time. ε_{it} is measured
117 by a longitudinal strain gauge glued at 330 mm from the sample interface and ε_{et} is measured
118 by a longitudinal strain gauge glued on the external face of the external output bar and at
119 295 mm from the confinement tube interface.

120



121

122 Figure 2 : Zoom on the mounting with the cell composed of the plug, the sample and the
 123 confinement tube (axisymmetric cut view).

124

125 The sample has a diameter $2R$ and a length L equal to 10 mm, the confinement tube
 126 has an external diameter $2R_t$ equal to 24 mm and the length scale is respected on Figure 2.
 127 The confinement tube and the plug, made of steel, have a Young's modulus E_t and a Poisson's
 128 ratio ν_t respectively equal to 200 GPa and to 0.29. The friction face of the confinement tube
 129 has been reamed and the sample was turned on a sliding lathe. Both have a weak surface
 130 roughness representative of the pyrotechnic structures roughness (arithmetic average of
 131 absolute values R_a roughly equal to 0.8). The radial clearance between the plug and the tube
 132 and between the internal output bar and the tube is of the order of 0.01 mm. Teflon sheets
 133 have been inserted between the plug and the sample and between the internal output bar and
 134 the sample in order to reduce the friction at these interfaces and thus increase the pressure at
 135 the tube-sample interface. The circumferential gauge glued on the confinement tube is 2 mm
 136 wide. The initial axial distance between the sample middle and the gauge middle is chosen
 137 equal to 2.5 mm because the sample displacement relatively to the tube during the test is
 138 supposed to be around 5 mm. Thus, the gauge is glued at the mean axial position of the
 139 sample middle.

140

141 The force F_i applied by the input bar on the plug and the velocity V_i at the input bar -
 142 plug interface can be determined from the Hopkinson formulae (2) and from strain waves ε_i
 143 and ε_r measured by the gauge and virtually transported at the input bar - plug interface (see
 144 Table 1 for symbols definitions):

145

$$146 \quad (2) \quad \begin{cases} F_i = -\pi R_i^2 E_i (\varepsilon_i + \varepsilon_r) \\ V_i = C_i (\varepsilon_r - \varepsilon_i) \end{cases}$$

147

148 The force F_{io} applied by the internal output bar on the sample and the velocity V_{io} at
 149 the internal output bar - sample interface can be determined from the Hopkinson formulae (3)
 150 and from strain wave ε_{it} measured by the gauge and virtually transported at the internal output
 151 bar - sample interface:

152

$$153 \quad (3) \quad \begin{cases} F_{io} = -\pi R_{io}^2 E_{io} \varepsilon_{it} \\ V_{io} = -C_{io} \varepsilon_{it} \end{cases}$$

154

155 The force F_{eo} applied by the external output bar on the confinement tube and the
 156 velocity V_{eo} at the external output bar – confinement tube interface can be determined from
 157 the Hopkinson formulae (4) and from strain wave ε_{et} measured by the gauge and virtually
 158 transported at the external output bar – confinement tube interface:

159

$$160 \quad (4) \quad \begin{cases} F_{eo} = \pi (R_{ieo}^2 - R_{eoo}^2) E_{eo} \varepsilon_{et} \\ V_{eo} = -C_{eo} \varepsilon_{et} \end{cases}$$

161

162 The equilibrium state of the cell (i.e. the confinement tube, the sample and the plug)
163 gives:

164

165 (5) $F_i = F_{eo} + F_{io}$

166

167 The stationary state of the cell gives:

168

169 (6) $V_i = V_{io}$

170

171 In the case of a stationary state, the sliding velocity at the friction interface V can be
172 expressed as following:

173

174 (7) $V = V_{io} - V_{eo}$ or $V = V_i - V_{eo}$

175

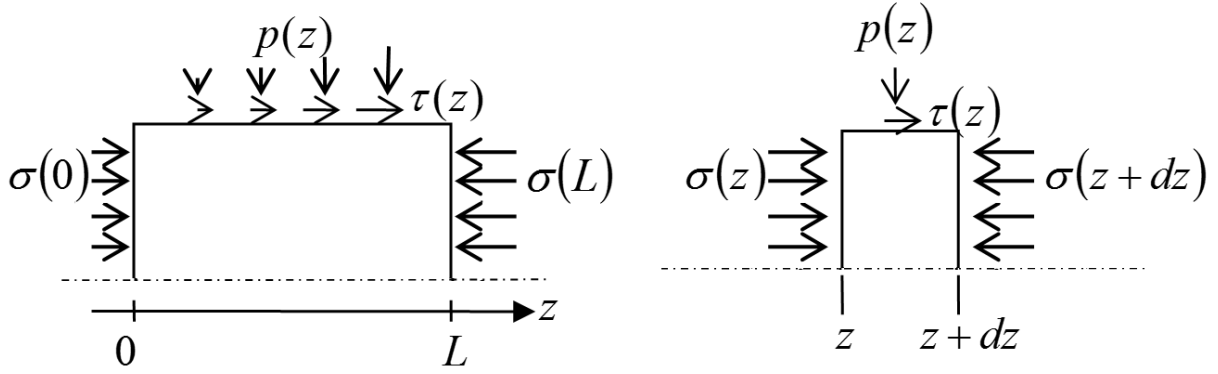
176 The sample behavior has to be modeled to obtain a second relation between the forces
177 F_i , F_{eo} and F_{io} . The model used is similar of the Janssen's one [19] and has been previously
178 used by the authors in [20] and [21]. The approach is based on three assumptions:

179 (i) the confinement tube is assumed to be perfectly rigid,

180 (ii) the sample behavior remains elastic,

181 (iii) in the sample, the axial, radial and circumferential stresses and strains do not depend on
182 the radial coordinate.

183



184

185 Figure 3: Stresses in the sample. z : axial coordinate, $p(z)$: radial pressure, $\tau(z)$: friction stress
 186 applied by the tube on the interface, $\sigma(z)$: axial stress.

187

188 If the stresses in the sample (Figure 3) are positive in compression and negative in
 189 traction, the Hooke's law leads to the following relation:

190

191 (8)
$$\frac{p(z)}{\sigma(z)} = \frac{\nu}{1-\nu}$$

192 ν being the II Poisson's ratio.

193

194 The axial equilibrium of the sample slice between z and $z+dz$ (Figure 3) leads to:

195

196 (9)
$$2\tau(z) = R\sigma'(z) = R \frac{d\sigma(z)}{dz}$$

197 R being the sample radius.

198

199 A Coulomb's law with a friction coefficient denoted f at the tube-sample interface
 200 leads to:

201

202 (10)
$$\tau(z) = f p(z)$$

203

204 The relations (8), (9) and (10) lead to a differential equation:

205

206 (11)
$$\frac{\sigma'(z)}{\sigma(z)} = \frac{2f\nu}{R(1-\nu)}$$

207

208 By taking into account the boundary conditions:

209

210 (12)
$$\begin{cases} F_i = \pi R^2 \sigma(L) \\ F_{io} = \pi R^2 \sigma(0) \end{cases}$$

211

212 we obtain:

213

214 (13)
$$\frac{F_i}{F_{io}} = \exp(\beta f) \text{ with } \beta = \frac{2\nu L}{R(1-\nu)}$$

215

216 The incident strain wave ε_i can be linked to the impact velocity of the striker V_s :

217

218 (14)
$$\varepsilon_i = -\frac{V_s}{2C_i}$$

219

220 Thanks to the Hopkinson formulae (2), (3) and (4), thanks to the equilibrium state

221 equation (5), thanks to the stationary state equation (6), and thanks to relation (13), the mean

222 pressure along the friction interface p_{mean} and the sliding velocity V can be determined from

223 the impact velocity of the striker V_s , from the friction coefficient f and from the set-up

224 parameters:

225

$$(15) \quad p_{mean} = \frac{R_i^2 R_{io}^2 E_i E_{io} [\exp(\beta f) - 1]}{2f R L [R_i^2 E_i C_{io} + R_{io}^2 E_{io} C_i \exp(\beta f)]} V_s$$

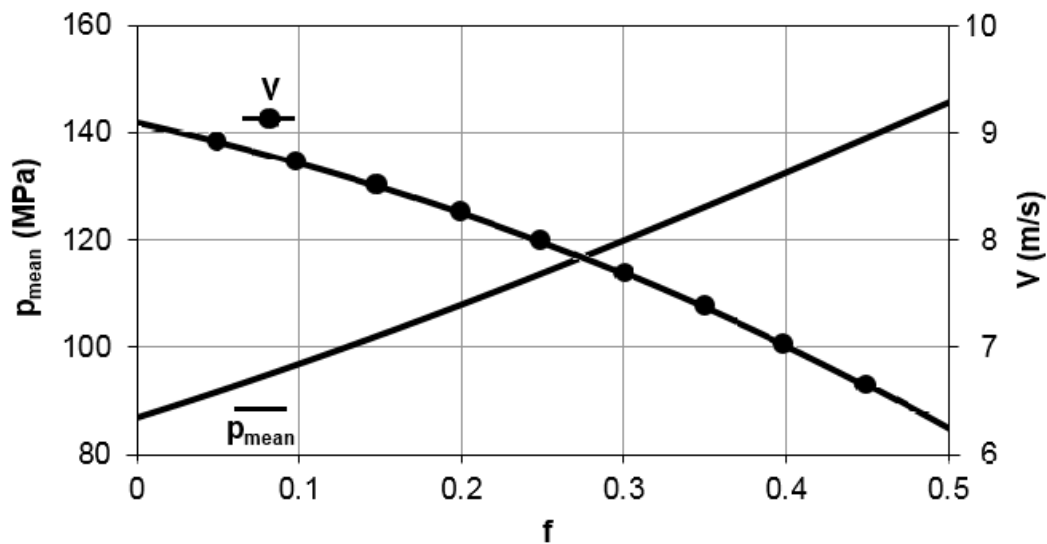
227

$$(16) \quad V = \frac{R_i^2 E_i \left\{ C_{io} - \frac{R_{io}^2 E_{io} C_{eo} [\exp(\beta f) - 1]}{(R_{eeo}^2 - R_{ieo}^2) E_{eo}} \right\}}{R_i^2 E_i C_{io} + R_{io}^2 E_{io} C_i \exp(\beta f)} V_s$$

229

230 Relations (15) and (16) enable to choose the apparatus dimensions (L , R , R_i , R_{io} , R_{eeo}
 231 and R_{ieo}), the apparatus materials (E_i , C_i , E_{io} , C_{io} , E_{eo} and C_{eo}) and the striker initial velocity V_s
 232 knowing the sample Poisson's ratio ν , the friction coefficient f and the desired interface
 233 solicitations (p_{mean} and V). It must be highlighted that an accurate calculation of the apparatus
 234 needs to know a priori an order of the friction coefficient f magnitude and needs to know
 235 accurately the sample Poisson's ratio ν . The striker of our apparatus can be launched at
 236 10 m/s. Figure 4 therefore displays the magnitudes of the mean pressure and of the sliding
 237 velocity that can be reached with our set-up. Figure 4 shows that the mean pressure increases
 238 and that the sliding velocity decreases when the friction coefficient increases. The desired
 239 100 MPa pressure and the desired 10 m/s sliding velocity can almost be simultaneously
 240 approached for very low friction coefficients (lower than 0.1). It could be noted that the
 241 pressure and the sliding velocity cannot be simultaneously imposed to a desired value because
 242 one depends on the other.

243



244

245 Figure 4 : Evolution of the mean pressure p_{mean} and of the sliding velocity V as a function of
 246 the friction coefficient f .

247

248 None of the former devices enables to reach such friction solicitations. The tribometer
 249 used in [20] enables to reach a sliding velocity of around 10 m/s but limits the mean pressure
 250 to 20 MPa whereas the tribometer used in [21] and in [22] enables to reach a mean pressure of
 251 around 100 MPa but limits the sliding velocity to 2 m/s.

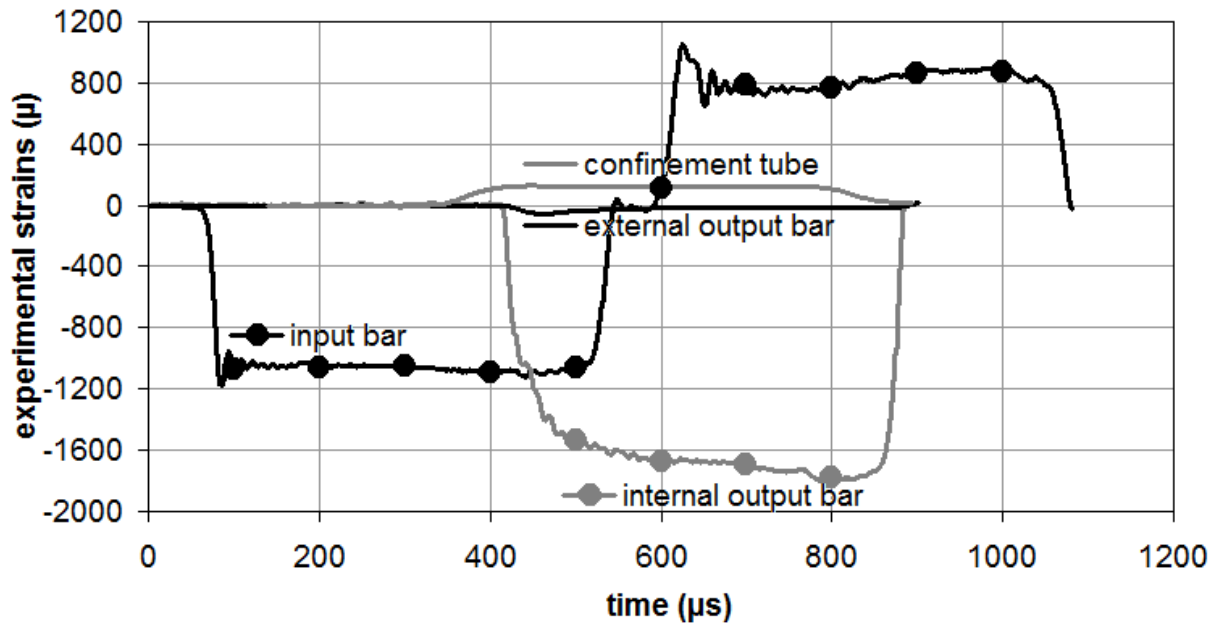
252

253 2.2 Analysis of measurements

254

255 A test has been conducted to experimentally check if the sample reaches a stationary
 256 equilibrium state as assumed in section 2.1. The time evolutions of the raw strains are shown
 257 on Figure 5. The forces applied by the bars on the cell and the velocities at the bars-cell
 258 interfaces are then determined from the Hopkinson formulae (2), (3) and (4). The input force
 259 can be compared to the output force on Figure 6 and the sample input velocity can be
 260 compared to the sample output velocity on Figure 7.

261



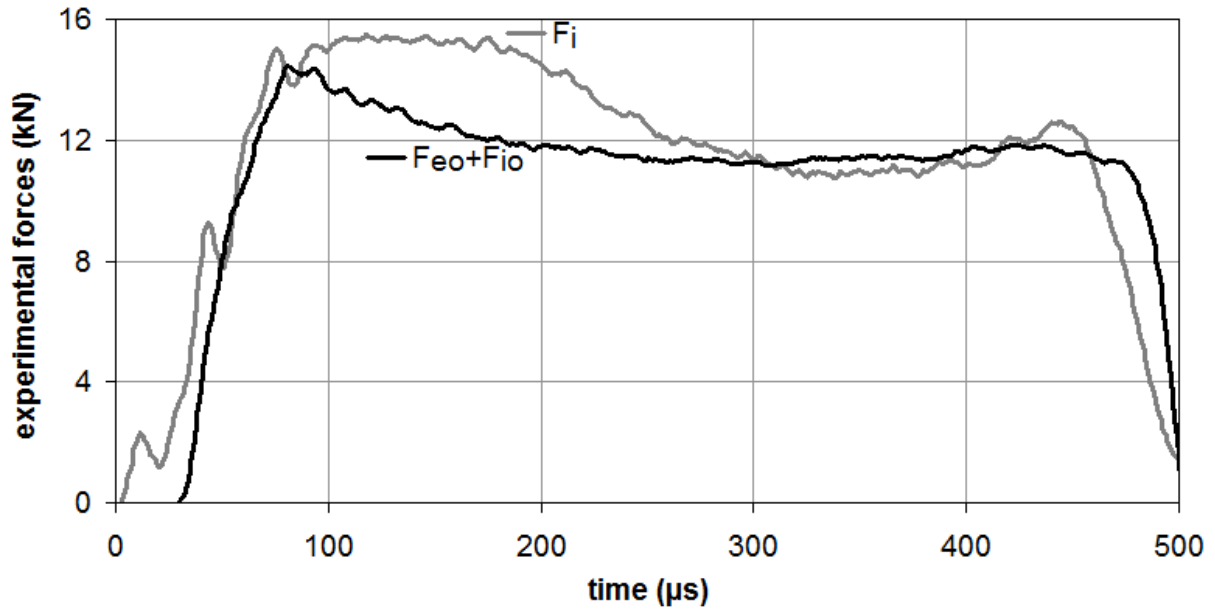
262

263 Figure 5: Time evolutions of the raw strains measured by the gauges glued on bars and on the
 264 confinement tube. The strain measured on the external output bar is very low compared to the
 265 others.

266

267 We can notice that the time beginning used on Figure 5 is different from the one used
 268 on the other figures and will be no more used in the paper.

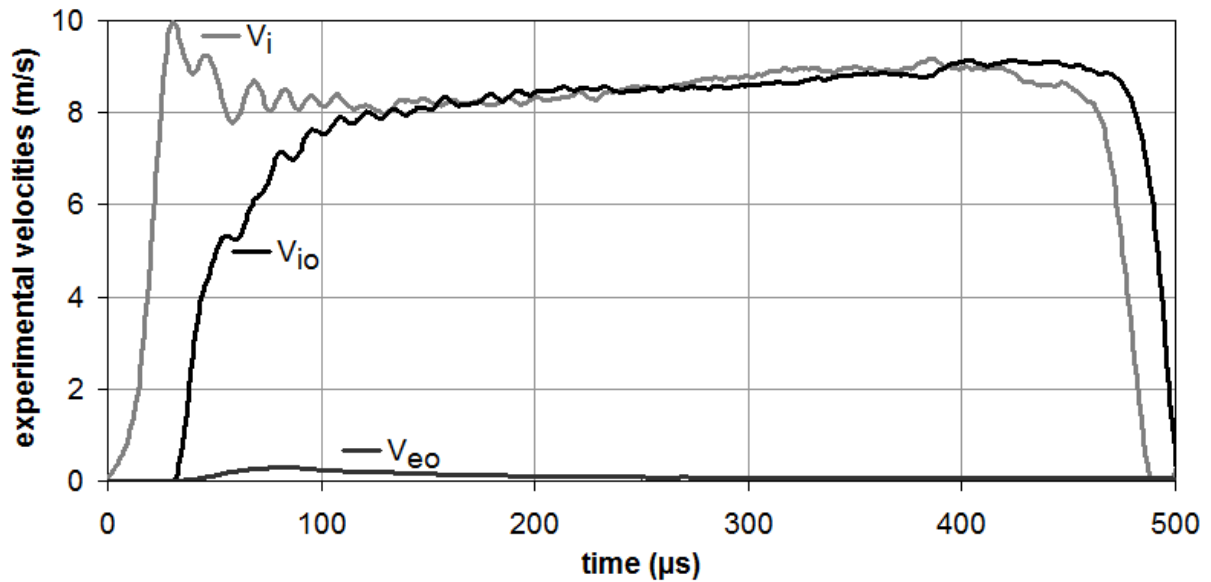
269



270

271 Figure 6: Time evolutions of the input force F_i and of the sum of the external output force and
 272 of the internal output force $F_{eo}+F_{io}$ deduced from the measured strain waves in the bars and
 273 from the Hopkinson formulae.

274

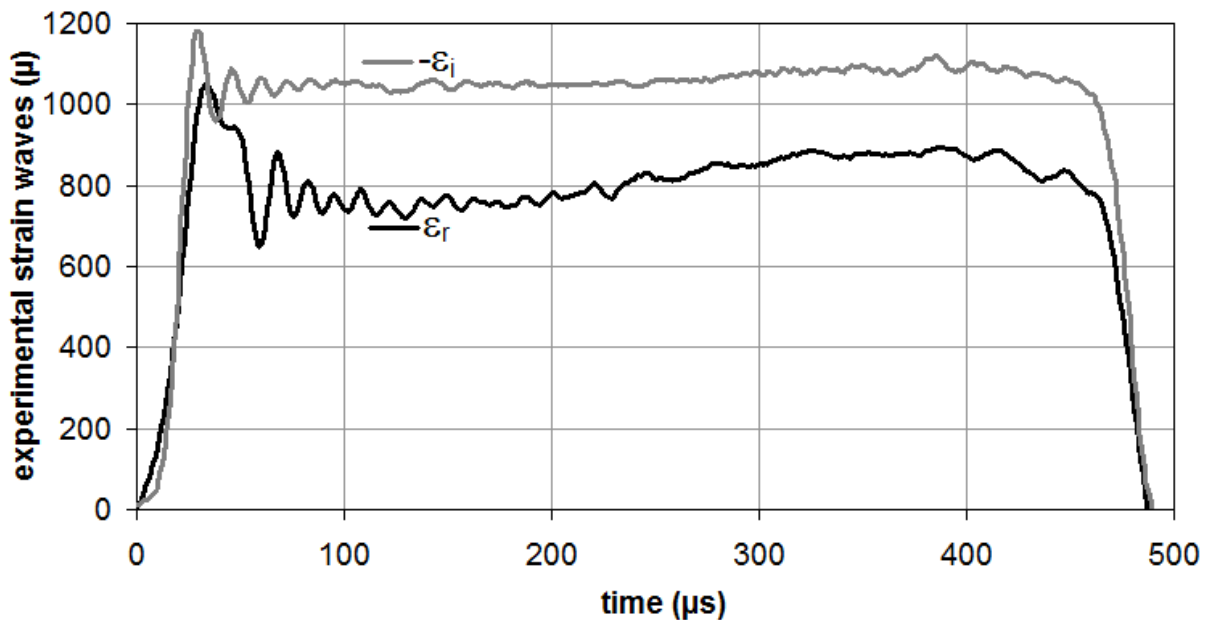


275

276 Figure 7: Time evolutions of the input velocity V_i , of the internal output velocity V_{io} and of
 277 the external output velocity V_{eo} deduced from the measured strain waves in the bars and from
 278 the Hopkinson formulae.

279

280 A quite satisfactory stationary equilibrium state can be observed on Figure 6 and
 281 Figure 7. The evolution of the experimental input force F_i during the transient phase (at the
 282 beginning) can be explained by the time shifting of the incident and the reflected waves ε_i and
 283 ε_r . These two waves being quasi-opposed (Figure 8), uncertainties are amplified when the
 284 input force is calculated with formula (2). The experimental evolution of F_i will therefore not
 285 be used to identify the friction coefficient f and we will focus only on the stationary phase
 286 (approximately from 300 μs to 400 μs).
 287



288
 289 Figure 8: Time evolutions of the opposite of the measured incident strain wave ε_i and of the
 290 measured reflected wave ε_r , both virtually transported at the input bar - plug interface.
 291

292 Figure 7 shows that the sliding velocity V is of the order of 8-9 m/s during the
 293 stationary phase.
 294

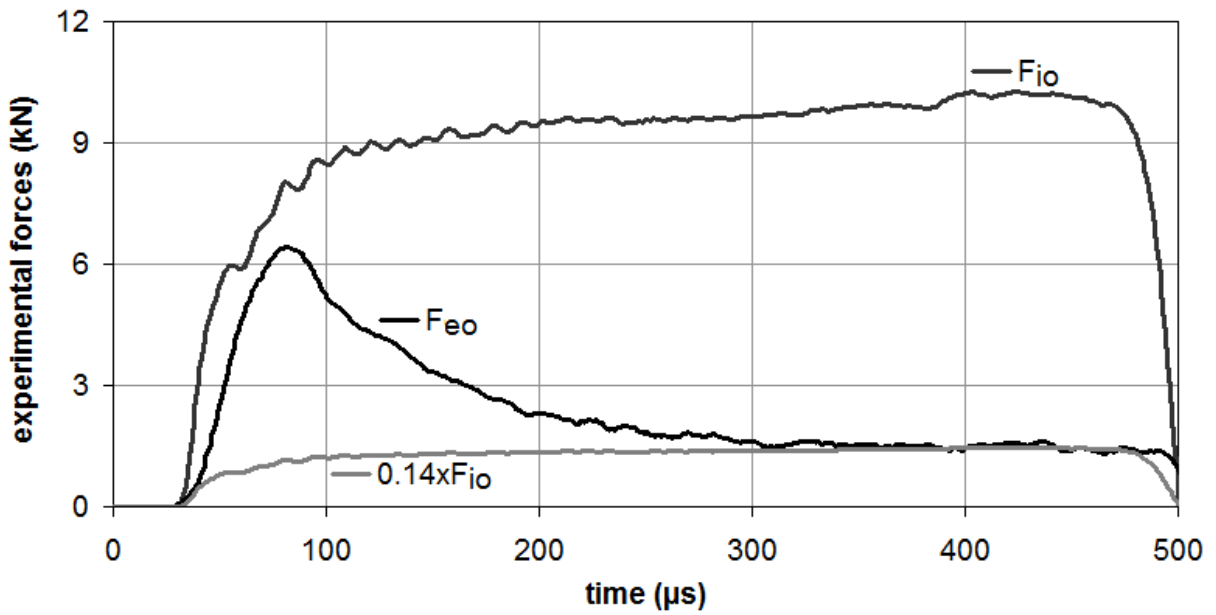
295 According to relations (5) and (13), the friction coefficient f can be deduced from the

296 output forces ratio $\frac{F_{eo}}{F_{io}}$:

297

$$298 \quad (17) \quad f = \frac{\ln\left(\frac{F_{eo}}{F_{io}} + 1\right)}{\beta}$$

299



300

301 Figure 9: Time evolutions of the external output force F_{eo} and of the internal output force F_{io}
 302 deduced from the measured strain waves in the bars and from the Hopkinson formulae.

303

304 The $\frac{F_{eo}}{F_{io}}$ ratio identified during the stationary phase on Figure 9 is roughly 0.14. By

305 using relation (17), it leads to $\beta f \approx 0.13$ and if $\nu \approx 0.4$ to $f \approx 0.05$.

306

307 The mean friction stress τ_{mean} can be deduced from F_{eo} which corresponds to the
 308 friction force:

309

310 (18) $\tau_{mean} = \frac{F_{eo}}{2\pi RL}$

311

312 The minimal pressure p_{min} is reached on $z = 0$ and the maximal pressure p_{max} in
313 reached on $z = L$ (Figure 3). According to relations (5), (8) and (12), p_{min} and p_{max} can be
314 expressed from the output forces F_{eo} and F_{io} :

315

316 (19)
$$\begin{cases} p_{min} = p(0) = \frac{\nu}{1-\nu} \frac{F_{io}}{\pi R^2} \\ p_{max} = p(L) = \frac{\nu}{1-\nu} \frac{F_{eo} + F_{io}}{\pi R^2} \end{cases}$$

317

318 According to relations (8), (9) and (10), the pressure p is an exponential function of
319 (fz):

320

321 (20)
$$p = p_{mean} \frac{\beta f \exp\left(\frac{\beta f z}{L}\right)}{\exp(\beta f) - 1}$$

322

323 For low magnitudes of f , p can thus be considered as an affine function of z , which
324 implies:

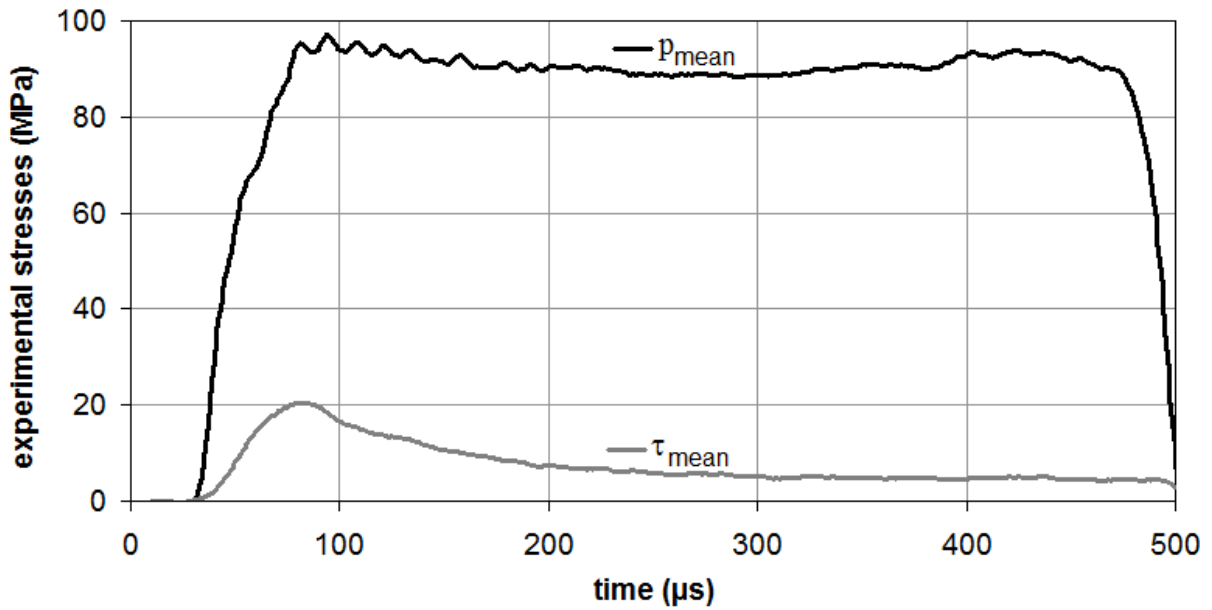
325

326 (21)
$$p_{mean} = \frac{p_{min} + p_{max}}{2}$$

327

328 The mean interface stresses are determined from the experimental output forces F_{eo}
329 and F_{io} , from relations (19) and from relation (21):

330



331

332 Figure 10: Time evolutions of the experimental mean pressure p_{mean} and of the experimental
333 mean friction stress τ_{mean} .

334

335 Figure 10 shows that the mean pressure p_{mean} is of the order of 90-100 MPa.

336

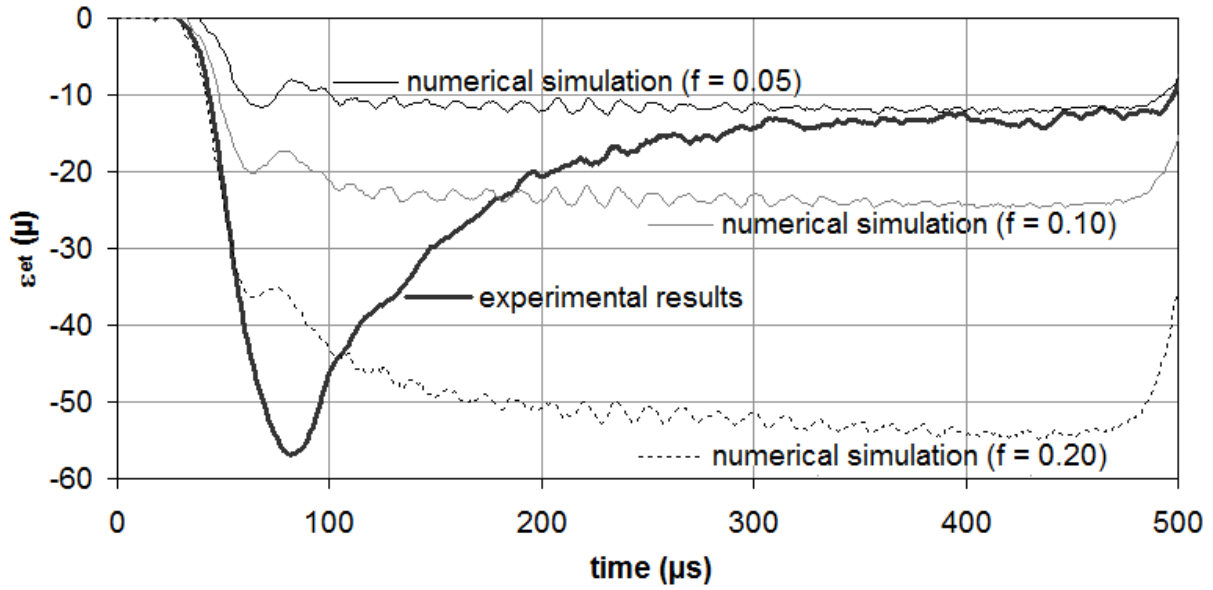
337 3 Numerical simulations of the test: check of the results consistency

338

339 Finite element simulations (software: ABAQUS/Explicit) are performed in order to
340 check the consistency of the experimental results and of the friction coefficient magnitude
341 identified from our analytical model ($f \approx 0.05$). The whole set-up except for the striker is
342 exactly reproduced in these simulations. As Teflon sheets have been inserted between the
343 plug and the sample and between the internal output bar and the sample, these contacts are
344 supposed to be frictionless. The experimental incident strain wave ε_i is used as an imposed
345 loading by applying on the right-hand extremity of the input bar (Figure 1) a pressure equal to
346 the opposite of the measured strain ε_i virtually transported at the extremity multiplied by the

347 input bar Young's modulus E_i . The opposite of ε_i can be seen on Figure 8. The strains ε_r , ε_{tu} ,
348 ε_{et} and ε_{it} can be considered as the mechanical response of the set-up to ε_i and the simulations
349 have been performed with several values of the friction coefficient f to study its influence on
350 the response.

351



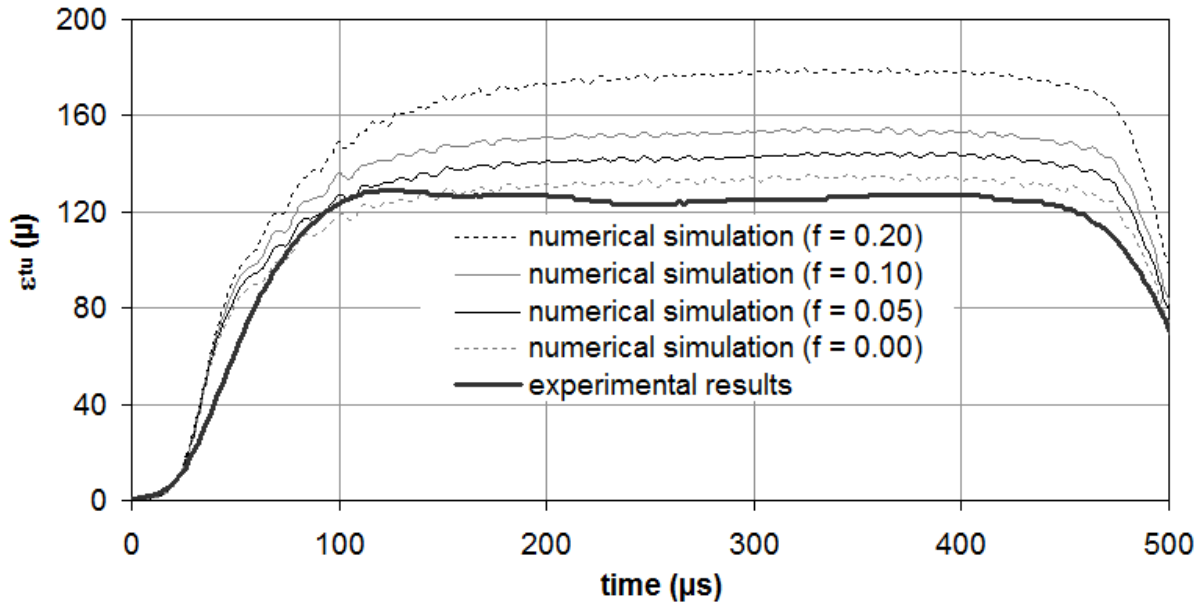
352

353 Figure 11: Time evolution of the measured external transmitted strain wave ε_{et} virtually
354 transported at the external output bar – confinement tube interface and its numerical
355 equivalent depending on the friction coefficient f magnitude.

356

357 The numerical equivalent of the strain measured by the gauge glued on the
358 confinement tube ε_{tu} is actually the mean value of the numerical circumferential strain along
359 the gauge width.

360

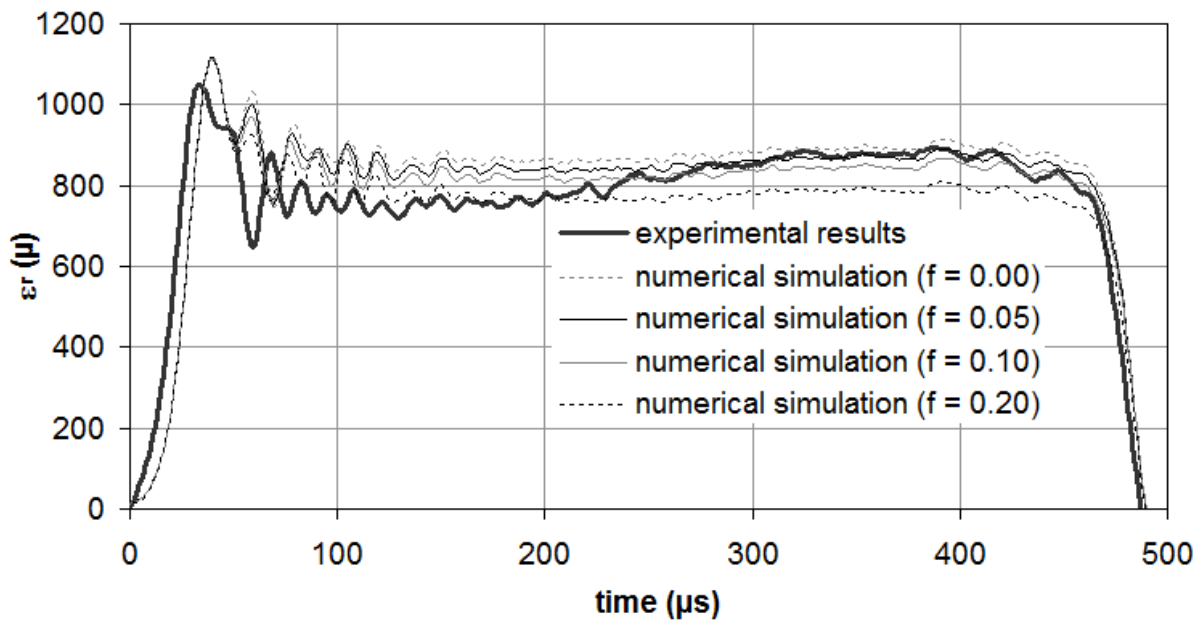


361

362 Figure 12: Time evolution of the strain measured by the gauge glued on the confinement tube

363 ε_{tu} and its numerical equivalent depending on the friction coefficient f magnitude.

364



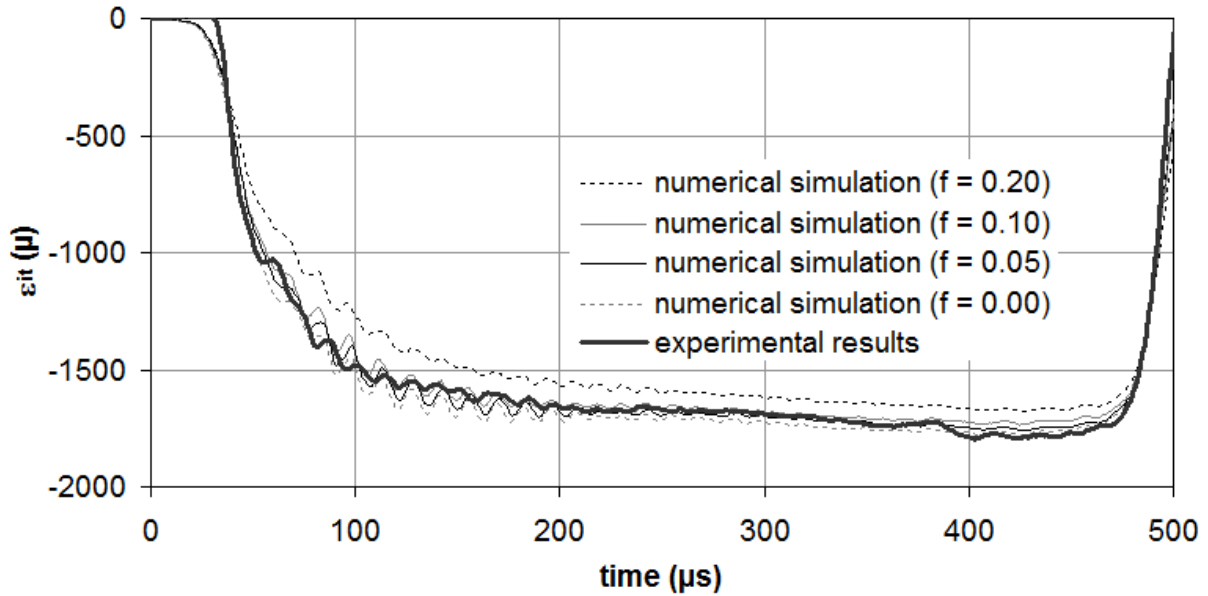
365

366 Figure 13: Time evolution of the measured reflected strain wave ε_r virtually transported at the

367 input bar - plug interface and its numerical equivalent depending on the friction coefficient f

368 magnitude.

369



370

371 Figure 14: Time evolution of the measured internal transmitted strain wave ε_{it} virtually
 372 transported at the internal output bar - sample interface and its numerical equivalent
 373 depending on the friction coefficient f magnitude.

374

375 The external transmitted strain wave ε_{et} is proportional to the friction force and is
 376 therefore the most friction dependent strain (Figure 11). During the stationary phase, $f = 0.05$
 377 is a very good fit with the experimental ε_{et} . The strain measured on the confinement tube ε_{tu} is
 378 also highly dependent on f , but a perfect fit cannot be obtained because of the numerical
 379 strains high values (Figure 12). The reflected strain wave ε_r and the internal transmitted strain
 380 wave ε_{it} are quasi-independent on friction (Figure 13 and Figure 14). During the stationary
 381 phase, $f = 0.05$ is consistent with the measured ε_r and with the measured ε_{it} .

382

383 4 Discussion of the analytical model assumptions

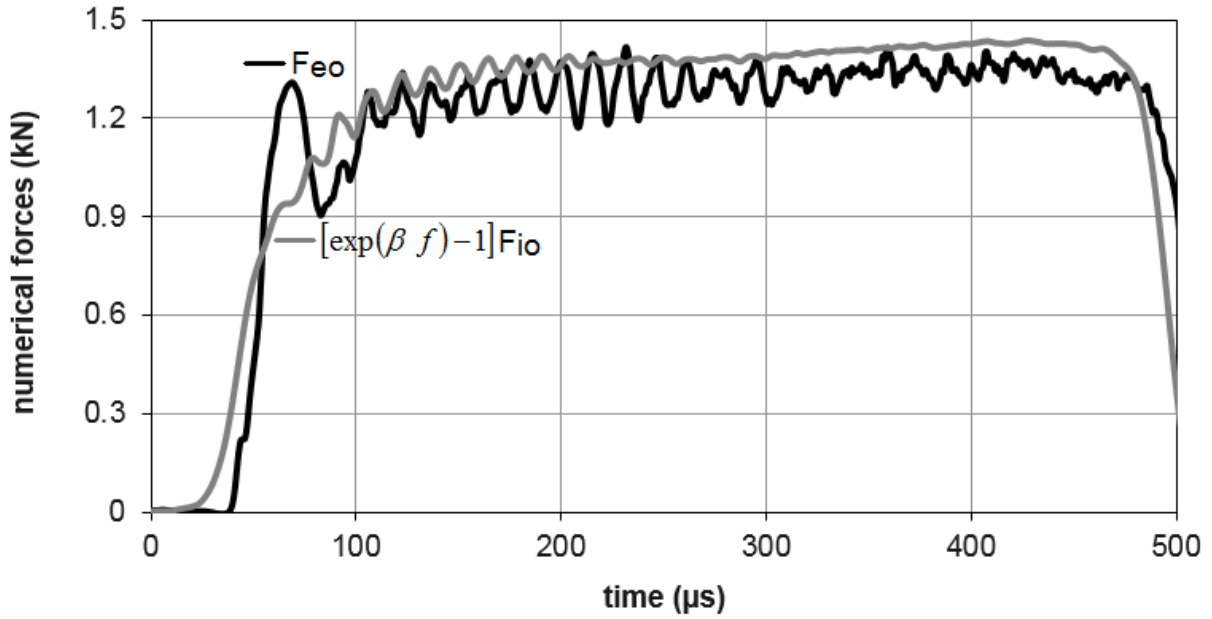
384

385 Relation (17) leads to the following one:

386

387 (22) $[\exp(\beta f) - 1]F_{io} = F_{eo}$

388



389

390 Figure 15: Time evolutions of the numerical external output force F_{eo} and of
 391 $[\exp(\beta f) - 1]F_{io}$ (with $f = 0.05$).

392

393 Figure 15 shows that the analytical model slightly overestimates the friction force F_{eo} .

394 Only this criterion finally matters because f is firstly identified from the $\frac{F_{eo}}{F_{io}}$ ratio.

395

396 5 Conclusion

397

398 The purpose was to design a set-up enabling the friction measurement between an inert
 399 material, mechanically representative of explosives, and a steel confinement. The desired
 400 sliding velocities and the desired pressures were respectively 10 m/s and 100 MPa. A
 401 confinement set-up using the split Hopkinson pressure bars technique had to be designed
 402 because of the low mechanical resistance of the inert material when submitted to the simple

403 compression of classical tribometers. Such a configuration does not enable to make direct
404 measurements. As a result, the stresses and the friction coefficient at the interface between
405 steel and the inert material were identified from indirect measurements, from an analytical
406 model and from the value of the inert material Poisson's ratio. It has been shown that the
407 sliding velocity and the pressure reached roughly 8-9 m/s and 90-100 MPa whereas the striker
408 was launched at only 10 m/s.

409

410 A very low friction coefficient has been measured: only 0.05. In [20] and [21], a
411 sliding velocity of the order of 1 mm/min has been imposed and the corresponding friction
412 coefficient is roughly 0.2. In [22], the mean pressure is approximately 70 MPa and the sliding
413 velocity is of the order of 2 m/s. In [20], the mean pressure is approximately 20 MPa and the
414 sliding velocity is around 10 m/s. In both cases, the friction coefficient is of the order of 0.4-
415 0.5. The reasons of such a variation should be studied in a future work. The friction drop at
416 the very beginning of the test could also be studied by using a time dependent friction model.

417

418 The measurements processing could also be improved by using an inverse method like
419 in [23]. Another prospect is the design of a compaction test enabling the friction force
420 measurement. Indeed, the study of the friction in compaction situations is an issue [16], [18]
421 and our device enables the simultaneous determination of the friction parameters and of the
422 compacted material parameters.

423

424 **Acknowledgments:** The authors would like to thank Maxime Biessy for his help and the
425 reviewers for their valuable comments.

426

427 **6 References**

428

429 [1]: Picart D, Delmaire-Sizes F, Gruau C, Trumel H. Ignition of a HMX-based PBX
430 submitted to impact: strain localisation and boundary condition. 16th Conference of the
431 American Physical Society Topical Group on Shock Compression of Condensed Matter
432 (2009).

433

434 [2]: Picart D, Bouton E. Non-shock ignition of a HMX-based high explosive: thermo-
435 mechanical numerical study. 14th International Detonation Symposium, Coeur d'Alène,
436 USA (2010).

437

438 [3]: Picart D, Ermisse J, Biessy M, Bouton E, Trumel H. Modelling and simulation of
439 plastic-bonded explosive mechanical initiation. *International Journal of Energetic
440 Materials and Chemical Propulsion*, 12(6), 487-509 (2013).

441

442 [4]: Field JE, Swallowe GM, Heaven SN. Ignition mechanisms of explosives during
443 mechanical deformations. *Proceeding of the Royal Society London A*, 383, 231-44
444 (1982).

445

446 [5]: Gruau C, Picart D, Belmas R, Bouton E, Delmaire-Sizes F, Sabatier J, Trumel H.
447 Ignition of a confined high explosive under low velocity impact. *International Journal of
448 Impact Engineering* 36, 537–550 (2008).

449

- 450 [6]: Vandersall KS, Chidester SK, Forbes JW, Garcia F, Greenwood DW, Switzer LL and
451 al. Experimental and modelling studies of crush, puncture, and perforation scenarios in
452 the Steven impact test. Office Naval Research 333-05-02, (Eds.), Proceedings of the
453 12th International Detonation Symposium, San Diego, 131–139 (2002).
- 454
- 455 [7]: Yodo A and al. Energetic materials for defense - Safety, vulnerability - Friability.
456 AFNOR NF EN 16701 (2014).
- 457
- 458 [8]: Kim HJ, Emge A, Winter RE, Keightley PT, Kim WK, Falk ML, Rigney DA.
459 Nanostructures generated by explosively driven friction: Experiments and molecular
460 dynamics simulations. *Acta Materiala*, 57(17), 5270-5282 (2009).
- 461
- 462 [9]: Rajagopalan S, Irfan MA, Prakash V. Novel experimental techniques for investigating
463 time resolved high speed friction. *Wear*, 225-229, Part 2, 1222-1237 (1999).
- 464
- 465 [10]: Huang H, Feng R. Dynamic Friction of SiC Surfaces: A Torsional Kolsky Bar
466 Tribometer Study. *Tribology Letters*, 27, 329-338 (2007).
- 467
- 468 [11]: Philippon S, Voyiadjis GZ, Faure L, Lodygowski A, Rusinek A, Chevrier P, Dossou E.
469 A Device Enhancement for the Dry Sliding Friction Coefficient Measurement Between
470 Steel 1080 and VascoMax with Respect to Surface Roughness Changes. *Experimental*
471 *Mechanics*, 51(3), 337-358 (2011).
- 472

473 [12]: Dickson PM, Parker GR, Smilowitz LB, Zucker JM, Asay BW. Frictional Heating and
474 Ignition of Energetic Materials. CP845, Conference of the American Physical Society
475 Topical Group on Shock Compression of Condensed Matter, 1057-1060 (2005).

476

477 [13]: Hoffman DM, Chandler JB. Aspect of the tribology of the plastic bonded explosive LX-
478 04. Propellants, Explosives, Pyrotechnics 29, 368–373 (2004).

479

480 [14]: Bailly P, Delvare F, Vial J, Hanus JL, Biessy M, Picart D. Dynamic behavior of an
481 aggregate material at simultaneous high pressure and strain rate: SHPB triaxial tests.
482 International Journal of Impact Engineering, 38, 73-84 (2011).

483

484 [15]: Forquin P, Safa K, Gary G. Influence of free water on the quasi-static and dynamic of
485 strength of concrete in confined compression tests. Cement and Concrete Research, 40,
486 321-333 (2009).

487

488 [16]: Azhdar B, Stenberg B, Kari L. Determination of dynamic and sliding friction, and
489 observation of stick-slip phenomenon on compacted polymers during high velocity
490 compaction. Polymer Testing, 25, 1069–1080 (2006).

491

492 [17]: Burlion N, Pijaudier-Cabot G, Dahan N. Experimental analysis of compaction of
493 concrete and mortar. International Journal for Numerical and Analytical Methods in
494 Geomechanics, 25(15), 1467-1486 (2001).

495

- 496 [18]: Yong-Ming Tien, Po-Lin Wu, Wei-Hsing Huang, Ming-Feng Kuo, Chen-An Chu. Wall
497 Friction measurement and compaction characteristics of bentonite powders. Powder
498 Technology 173, 140-151 (2007).
499
- 500 [19]: Janssen HA. Versuche über Getreiedruch in Silozellen. Vereins Z Deutsch Eng 39, 1045
501 (1895).
502
- 503 [20]: Durand B, Delvare F, Bailly P, Picart D. Friction between steel and a confined inert
504 material representative of explosives under severe loadings. Experimental Mechanics
505 DOI 10.1007/s11340-014-9885-z (2014).
506
- 507 [21]: Durand B, Delvare F, Bailly P, Picart D. Identification of the friction under high
508 pressure between an aggregate material and steel: experimental and modelling aspects.
509 International Journal of Solids and Structures, 50(24), 4108-4117 (2013).
510
- 511 [22]: Durand B, Delvare F, Bailly P, Picart D. A friction test between steel and a brittle
512 material at high contact pressures and high sliding velocities. 10th International
513 DYMAT Conference (2012).
514
- 515 [23]: Durand B, Delvare F, Bailly P. Numerical solution of Cauchy problems in linear
516 elasticity in axisymmetric situations. International Journal of Solids and Structures, 21,
517 3041-3053 (2011).
518